DOI: 10.13009/EUCASS2017-97

7TH EUROPEAN CONFERENCE FOR AERONAUTICS AND AEROSPACE SCIENCES (EUCASS)

DOI: ADD DOINUMBER HERE

Effect of Vibrational Temperature Boundary Condition of Isothermal Wall on Hypersonic Shock Wave Laminar Boundary Layer Interaction of a Hollow Cylinder Flare

Nadia Kianvashrad[⋆] *and Doyle Knight*[⋆†]
[⋆]*Rutgers - The State University of New Jersey*
New Brunswick, New Jersey 08903, USA
nadiakianvashrad@gmail.com · doyleknight@gmx.com
[†]Corresponding author

Abstract

The effect of the vibrational temperature boundary condition at an isothermal wall on prediction of aerothermodynamic loading of hypersonic laminar flow over a hollow cylinder flare is examined for Mach numbers from 12.6 to 13.2 and stagnation enthalpies from 10.43 to 21.85 MJ/kg. Two vibrational boundary conditions considered here are 1) $T_\alpha^{\text{vib}}\big|_w = T_w$ and 2) $(\partial T_\alpha^{\text{vib}}/\partial n)\big|_w = 0$. The variation of the predicted peak surface heat transfer and surface pressure due to the change in the vibrational temperature boundary condition at the isothermal wall is negligible.

1. Introduction

There is a recent reinterest in hypersonic flight. This renewed interest is evident by the numerous programs around the world to produce a hypersonic flight vehicle. The DF-ZF Hypersonic Glide Vehicle (HGV), the Force Application and Launch from CONtinental United States (FALCON), the High-Speed Experimental Fly Vehicles (HEXAFLY) and HEXAFLY - International (HEXAFLY-INT), the Hypersonic International Flight Research Experimentation (HIFiRE), the Hypersonic Technology Demonstrator Vehicle (HSTDV), the SHarp Edge Flight Experiment (SHEFEX), the Scramjet Powered Accelerator for Reusable Technology Advancement (SPARTAN), and the Experimental Spaceplane (XS-1) are some examples.

At hypersonic speeds, the interaction of shock waves and the boundary layer of the body creates localized high pressure and high temperature regions. Accurate prediction of aerothermodynamic loading is essential for designing of hypersonic vehicles. For example, in the reentry of Space Shuttle flight STS-1, the body flap was extended to 14°, exceeding the planned 8° to 9° which was required for pitch control.[3,19] Postflight analysis of the longitudinal trim characteristics demonstrated that the computational fluid dynamic (CFD) predictions of pitch trim were in error. This error was a result of inaccurate prediction of the pressure distribution due in part to the effects of shock wave boundary layer interactions caused by the body flap deployment.

Several researches have focused on prediction of aerothermodynamic loading in laminar hypersonic flows. Among these are reviews in recent years by Harvey,[9] Knight,[15] Candler,[4] and Gaitonde[7] and Knight *et al*.[14] A blind study was presented at the AIAA AVIATION 2014 meeting in Atlanta, GA based on the experiments performed at the Calspan University of Buffalo Research Center (CUBRC) for double cone and hollow cylinder flare configurations.[17,18] There are several differences between the computational results and experiments especially in the prediction of peak pressure and heat transfer and separation length. Kianvashrad and Knight[10–13] examined different models to understand the reason of this discrepancy. They reported that vibrational-translational energy exchange has a negligible effect while the temperature dependency of specific heat and transport data models have a significant effect on the prediction of peak surface pressure and heat transfer.[13] Moreover, they compare the results of a perfect gas model and a non-equilibrium calculation with Park I thermochemistry and find out that the perfect gas model predicts the peak heat transfer within twice the experimental uncertainty and in lower enthalpy cases, even better prediction of surface heat transfer achieved by the perfect gas model than Park I model.[11] Knowing that GASP software - used for part of their calculation - has a different boundary condition for vibrational temperature at an isothermal wall[2] than their C^{++} code, it is essential to find out what is the effect of the different vibrational boundary condition on the prediction of surface pressure and heat transfer.

DOI: 10.13009/EUCASS2017-97

The objective of this research is to examine the effects of the difference between vibrational temperature boundary conditions at an isothermal wall on the prediction of surface heat transfer and surface pressure for a hollow cylinder flare under laminar flow conditions. The related experiments for the hollow cylinder flare were performed at CUBRC.

2. Description of Experiment

The experimental model shown in Fig. 1 is 220 mm in overall length. Eighteen pressure transducers and fifty-one heat transfer gauges are mounted on the hollow cylinder and flare surface. Five separate runs were conducted in the LENS XX expansion tunnel at stagnation enthalpies from 5.07 MJ/kg to 21.85 MJ/kg and Mach numbers from 11.3 to 13.2. The specific experiments considered in this paper are listed in Table 1. The Reynolds numbers (based on freestream conditions and the length of the hollow cylinder) range from 11,826 to 42,284 thereby assuring a fully laminar flow. The inflow gas was air in full chemical and thermochemical equilibrium with mass fractions of 0.765 and 0.235 for N_2 and O_2, respectively. The model surface is isothermal at 300 K. Details of the LENS XX facility are presented in Dufrene *et al*.[5,6]

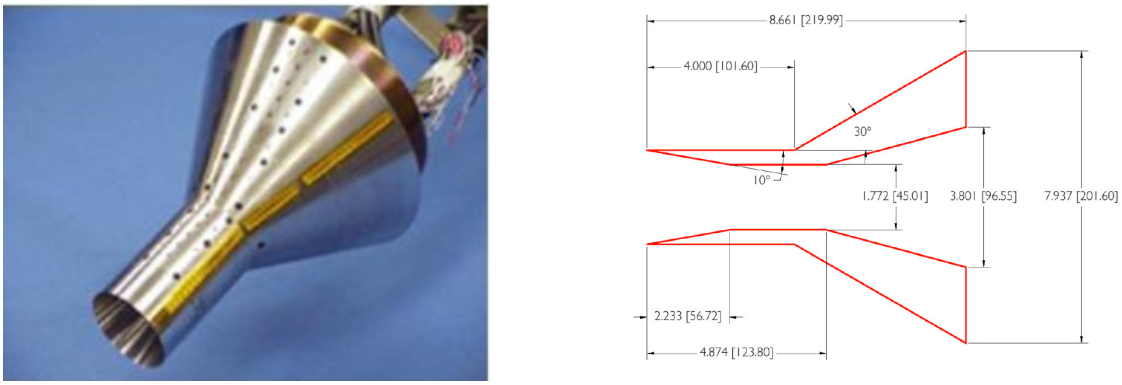

(a) Instrumentation (b) Geometry

Figure 1: Small Hollow Cylinder Flare (dimensions in inches [mm])

Table 1: Flow Conditions

Run No.	Total Enthalpy (MJ/kg)	Mach Number	Pitot Pressure (kPa)	Unit Reynolds ($/10^6$ m^{-1})	Velocity (km/s)	Density (g/m^3)	Temperature (K)
2	10.43	12.6	9.7	0.12	4.497	0.499	318
5	21.85	13.2	39.0	0.20	6.515	0.947	618

3. Methodology

The governing equations are the non-equilibrium compressible viscous laminar Navier-Stokes equations. We consider a reacting mixture of gases with density ρ_α for $\alpha = 1, \ldots, n$ of which $\alpha = 1, \ldots, m$ constitute diatomic (or polyatomic) species and the remainder ($i = m+1, \ldots, n$) represent monatomic species.

Conservation of Mass

The conservation of mass is

$$\frac{\partial \rho_\alpha}{\partial t} + \frac{\partial \rho_\alpha u_j}{\partial x_j} = \dot{\omega}_\alpha^{\text{spe}} + \frac{\partial}{\partial x_j}\left[\rho D \frac{\partial Y_\alpha}{\partial x_j}\right] \quad \text{for } \alpha = 1, \ldots, n \tag{1}$$

where ρ_α is the density of species α, the mass-averaged velocity is u_j, and ρ is the mixture density

$$\rho = \sum_{\alpha=1}^{N} \rho_\alpha \tag{2}$$

DOI: 10.13009/EUCASS2017-97

The mass fraction is defined as

$$Y_\alpha = \frac{\rho_\alpha}{\rho} \tag{3}$$

The rate of production of species α is denoted as $\dot{\omega}_\alpha^{\text{spe}}$ and defined as

$$\dot{\omega}_\alpha^{\text{spe}} = \mathcal{M}_\alpha \sum_{j=1}^{J} \left(\nu''_{\alpha,j} - \nu'_{\alpha,j}\right) k_{f,j} \left[\prod_{l=1}^{n} \left(\frac{\rho_l}{\mathcal{M}_l}\right)^{\nu'_{l,j}} - \frac{1}{k_{e,j}} \prod_{l=1}^{n} \left(\frac{\rho_l}{\mathcal{M}_l}\right)^{\nu''_{l,j}}\right] \quad \text{for } \alpha = 1, \ldots, n \tag{4}$$

for the general reaction expressions

$$\nu'_{1,j} X_1 + \ldots + \nu'_{n,j} X_n \rightleftharpoons \nu''_{1,j} X_1 + \ldots + \nu''_{n,j} X_n \quad \text{for } j = 1, \ldots, J \tag{5}$$

where J is the number of reactions, and $\nu'_{\alpha,j}$ and $\nu''_{\alpha,j}$ are the stoichiometric coefficients of the reactants and species X_α in the j^{th} reaction.

The diffusion of species is modeled by Fick's Law assuming a uniform diffusivity D defined by

$$D = \frac{\mu}{\rho Sc} \tag{6}$$

where $Sc = 0.7$ is the constant Schmidt number and μ is the molecular viscosity.

Conservation of Momentum

The conservation of momentum is

$$\frac{\partial \rho u_i}{\partial t} + \frac{\partial \rho u_i u_j}{\partial x_j} = -\frac{\partial p}{\partial x_i} + \frac{\partial \tau_{ij}}{\partial x_j} \quad \text{for } i = 1, 2, 3 \tag{7}$$

where the laminar viscose stress tensor,τ_{ij}, is

$$\tau_{ij} = -\tfrac{2}{3}\mu \frac{\partial u_k}{\partial x_k} \delta_{ij} + \mu \left(\frac{\partial u_i}{\partial x_j} + \frac{\partial u_j}{\partial x_i}\right) \tag{8}$$

Conservation of Total Energy

The total energy per unit mass ε is the sum of the internal energy per unit mass e and the kinetic energy per unit mass

$$\varepsilon = e + \tfrac{1}{2} u_j u_j \tag{9}$$

The internal energy per unit mass e is the sum of the internal energies of each of the n species

$$e = \sum_{\alpha=1}^{n} \frac{\rho_\alpha}{\rho} e_\alpha \tag{10}$$

where the internal energy per unit mass of each species e_α is the sum of an equilibrium internal energy $e_\alpha^{\text{eq}}(T)$ due to random translational energy and rotational energy (in the case of molecules) at a bulk equilibrium temperature T and a non-equilibrium internal energy $e_\alpha^{\text{vib}}(T_\alpha^{\text{vib}})$ due to vibrational excitation (in the case of molecules)

$$e_\alpha = e_\alpha^{\text{eq}}(T) + e_\alpha^{\text{vib}}(T_\alpha^{\text{vib}}) \tag{11}$$

The equilibrium internal energy of species α is

$$e_\alpha^{\text{eq}}(T) = h_{f_\alpha}^o + \int_{T_{\text{ref}}}^{T} c_{v_\alpha}(T)\, dT \tag{12}$$

The conservation of total energy is

$$\frac{\partial \rho \varepsilon}{\partial t} + \frac{\partial}{\partial x_j}\left(\rho\varepsilon + p\right) u_j = -\frac{\partial q_j}{\partial x_j} + \frac{\partial \tau_{ij} u_i}{\partial x_j} \tag{13}$$

where the heat transfer vector is

$$q_j = -k\frac{\partial T}{\partial x_j} - \sum_{\alpha=1}^{m} k_\alpha^{\text{vib}} \frac{\partial T_\alpha^{\text{vib}}}{\partial x_j} - \sum_{\alpha=1}^{n} \rho h_\alpha D_\alpha \frac{\partial Y_\alpha}{\partial x_j} \tag{14}$$

DOI: 10.13009/EUCASS2017-97

The static enthalpy per unit mass for species α is

$$h_\alpha = h^o_{f_\alpha} + \int_{T_{\text{ref}}}^{T} c_{p_\alpha}(T)\, dT \tag{15}$$

where $h^o_{f_\alpha}$ is the enthalpy of formation of species α at T_{ref}.

Conservation of Vibrational Energy

The conservation of vibrational energy is

$$\frac{\partial \rho_\alpha e^{\text{vib}}_\alpha}{\partial t} + \frac{\partial \rho_\alpha e^{\text{vib}}_\alpha u_j}{\partial x_j} = -\frac{\partial q^{\text{vib}}_{\alpha_j}}{\partial x_j} + \dot{\omega}^{\text{vib}}_\alpha \quad \text{for } \alpha = 1, \ldots, m \tag{16}$$

The vibrational temperature for a molecule with a single characteristic temperature of vibration $\Theta^{\text{vib}}_\alpha$ is

$$T^{\text{vib}}_\alpha = \frac{\Theta^{\text{vib}}_\alpha}{\log\left(\frac{R_\alpha \Theta^{\text{vib}}_\alpha}{e^{\text{vib}}_\alpha} + 1\right)} \tag{17}$$

where R_α is given by Eq. 27.

The vibrational heat transfer vector is

$$q^{\text{vib}}_{\alpha_j} = -k^{\text{vib}}_\alpha \frac{\partial T^{\text{vib}}_\alpha}{\partial x_j} - \rho D_\alpha e^{\text{vib}}_\alpha \frac{\partial Y_\alpha}{\partial x_j} \tag{18}$$

The source term is

$$\dot{\omega}^{\text{vib}}_\alpha = \rho_\alpha \dot{e}^{\text{vib}}_\alpha + \dot{\omega}^{\text{spe}}_\alpha e^{\text{vib}}_\alpha \tag{19}$$

where $\dot{e}^{\text{vib}}_\alpha$ is the translational-vibrational energy transfer per unit mass of species α. We consider the classical Landau-Teller model[23]

$$\dot{e}^{\text{vib}}_\alpha = \frac{e^{\text{vib}^*}_\alpha(T) - e^{\text{vib}}_\alpha(T^{\text{vib}}_\alpha)}{\tau_\alpha} \tag{20}$$

where $e^{\text{vib}^*}_\alpha$ is the equilibrium vibrational energy per unit mass of species α defined by

$$e^{\text{vib}^*}_\alpha(T) = \sum_{n=1}^{N_{\Theta,\alpha}} \frac{R_\alpha \Theta^{\text{vib}\,(n)}_\alpha}{\exp(\Theta^{\text{vib}\,(n)}_\alpha / T) - 1} \tag{21}$$

and $N_{\Theta,\alpha}$ is the number of characteristic temperatures $\Theta^{\text{vib}\,(n)}_\alpha$ and τ_α is the relaxation time[20] of species α defined by

$$\tau_\alpha = \frac{\sum_{\beta=1}^{n} M_\beta}{\sum_{\beta=1}^{n} M_\beta \tau^{-1}_{\alpha\beta}} \tag{22}$$

where $M_\alpha = \rho_\alpha / \mathcal{M}_\alpha$ is the molar concentration of species α and $\tau_{\alpha\beta}$ is the characteristic relaxation time of species α resulting from collisions with species β defined by[20]

$$\tau_{\alpha\beta} = \frac{1}{p} \exp\left[A_{\alpha\beta}\left(T^{-\frac{1}{3}} - B_{\alpha\beta}\right) - 18.42\right] \tag{23}$$

where $\tau_{\alpha\beta}$ is in seconds and p is in atmospheres, and

$$A_{\alpha\beta} = 0.00116\, \mathcal{M}^{\frac{1}{2}}_{\alpha\beta} \Theta^{\text{vib}\,\frac{4}{3}}_\alpha \quad \text{and} \quad B_{\alpha\beta} = 0.015\, \mathcal{M}^{\frac{1}{4}}_{\alpha\beta} \tag{24}$$

and the averaged molecular weight is defined by

$$\mathcal{M}_{\alpha\beta} = \frac{\mathcal{M}_\alpha \mathcal{M}_\beta}{\mathcal{M}_\alpha + \mathcal{M}_\beta} \tag{25}$$

where $\mathcal{M}_\alpha$ is the molecular weight of species α.

Equation of State

The equation of state is

$$p = T \sum_{\alpha=1}^{n} \rho_\alpha R_\alpha \tag{26}$$

DOI: 10.13009/EUCASS2017-97

where the gas constant R_α for each species is

$$R_\alpha = \frac{\mathcal{R}}{\mathcal{M}_\alpha} \tag{27}$$

where $\mathcal{R}$ is the Universal Gas Constant.

Thermodynamic Data and Transport Properties

The species thermodynamic data and species transport properties are obtained from Gupta, Yos, Thompson and Lee[8] (NASA-RP-1232) database. The mixture viscosity μ and thermal conductivity k are determined by Wilke's Rule.[24] The Prandtl number $Pr = 0.72$ and Schmidt number $Sc = 0.7$. The vibrational thermal conductivity of species α is

$$k_\alpha^{\text{vib}} = \mu_\alpha R_\alpha \tag{28}$$

where μ_α and R_α are the molecular viscosity and gas constant for species α, respectively.

Thermochemistry Model

The simulations represented in this paper assume $\dot{\omega}_\alpha^{\text{spe}} = 0$ which means there is no thermochemistry for these calculations.

Boundary Conditions

The computational domain is shown in Fig. 2. Symmetry boundary conditions are applied from A to B. The outer surface of the hollow cylinder flare (B to C) is no slip with $T = T_w$ and non-catalytic ($\partial Y_\alpha/\partial n = 0$ where n is the normal distance to the boundary). Zero gradient outflow boundary conditions are applied on C to D. Uniform freestream conditions are imposed on A to E and E to D.

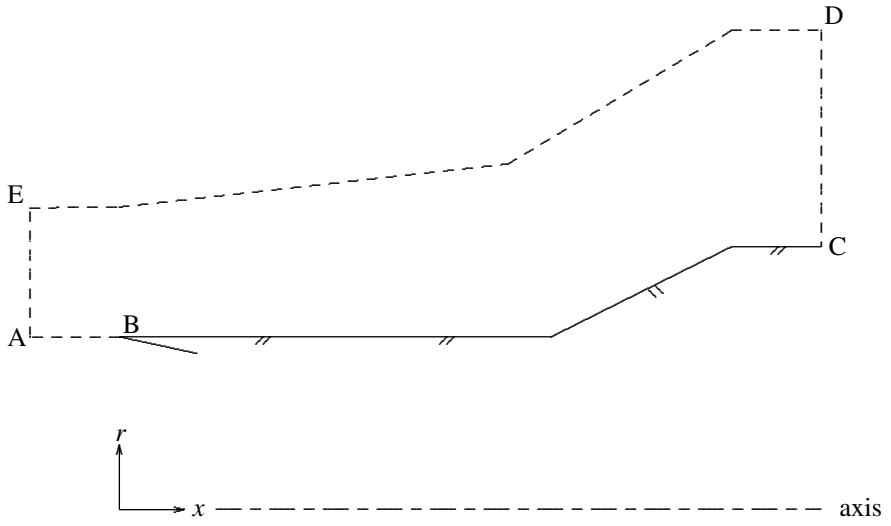

Figure 2: Computational domain

Vibrational Energy Boundary Condition for No-Slip Isothermal Wall

The no-slip isothermal wall boundary condition is divided into two different models due to differences in vibrational energy condition between the literature and GASP software. The first vibrational boundary condition is[21]

$$e_\alpha^{\text{vib}}\Big|_w = e_\alpha^{\text{vib}}(T_w) \quad \text{or} \quad T_\alpha^{\text{vib}}\Big|_w = T_w \tag{29}$$

which is denoted "fixed" and the second vibrational boundary condition is[1]

$$\left(\frac{\partial e_\alpha^{\text{vib}}}{\partial n}\right)\Bigg|_w = 0 \quad \text{or} \quad \left(\frac{\partial T_\alpha^{\text{vib}}}{\partial n}\right)\Bigg|_w = 0 \tag{30}$$

denoted "zero gradient".

Numerical Algorithm

The governing equations were solved by a finite volume code developed by the authors using a block structured grid. The inviscid fluxes are discretized using the Roe's method[22] with the second-order Monotone Upstream Scheme

DOI: 10.13009/EUCASS2017-97

for Conservation Laws[16] (MUSCL) reconstruction. Viscous fluxes are discretized using the second-order central differencing. The Data Parallel Line Relaxation (DPLR) of Wright *et al*[25] is incorporated to achieve high computational efficiency with Courant numbers up to several hundred. The C++ code is parallelized using Message Passing Interface (MPI). The simulations are initialized using the freestream conditions and converged to steady state. The grid of 0.6 M cells is used for this calculation with the grid properties given in Table 2.

Table 2: Grid properties

$\Delta\xi$ (μm)	$\Delta\eta_{min}$ (μm)	$\Delta\zeta$ ($degree$)
461	50	2.5

NOTE:
$\Delta\xi$ is spacing along the wall
$\Delta\eta$ is spacing normal to the wall
$\Delta\zeta$ is the axial spacing

4. Results

We consider two series of vibrationally-nonequilibrium simulations of hollow cylinder flare with "fixed" and "zero gradient" vibrational temperature boundary condition at isothermal wall defined in Section 3. The calculations with fixed vibrational boundary condition are denoted "Vibrationally non-equilibrium - fixed" and the calculations with zero gradient vibrational boundary condition are denoted as "Vibrationally non-equilibrium - gradient". Table 3 presents the specifications of each model.

Table 3: Models Specifications

Model	Modification to governing equations		Transport Properties				Vibrational condition in Isothermal BC
	$\dot{\omega}_\alpha^{\text{spe}}$	$\dot{\omega}_\alpha^{\text{vib}}$	Specific heat	Viscosity	Pr	Sc	
Vibrationally non-equilibrium - fixed	0	$\rho_\alpha \dot{e}_\alpha^{\text{vib}}$	Gupta *et. al* database	and Wilke's rule	0.72	0.7	Fixed
Vibrationally non-equilibrium - gradient	0	$\rho_\alpha \dot{e}_\alpha^{\text{vib}}$	Gupta *et. al* database	and Wilke's rule	0.72	0.7	zero gradient

The results section is divided into two subsections: comparison with experiments and analysis of flow structure.

4.1 Comparison with Experiments

In this section the surface heat transfer and surface pressure of each case is compared with the experimental data. The purpose of these comparisons between numerical and experimental results is understanding the effect of the vibrational energy boundary condition at the isothermal wall on prediction of surface pressure and heat transfer. It should be noted here that the surface heat transfer calculation does not include the vibrational heat transfer.

The computed and experimental surface pressure and heat transfer of Run 2 (10.43 MJ/kg) are shown in Fig. 3. The zero gradient boundary condition leads to a negligible increase in the peak surface heat transfer compared to the fixed boundary condition. The rise in the surface heat transfer is started slightly earlier for the zero gradient boundary condition. There is almost no effect on surface pressure as a consequent of changing the boundary condition but a very small change in the shape of the peak region.

The comparison of surface heat transfer and surface pressure of Run 5 (21.85 MJ/kg) of fixed and zero gradient boundary conditions of vibrational temperature at the isothermal wall are shown in Fig 4. There is a small increase in the peak surface heat transfer due to change of vibrational boundary condition from fixed to zero gradient. Moreover, the rise of surface heat transfer starts slightly earlier for the zero gradient vibrational boundary condition. The surface heat transfer at the end of the flare is higher for the zero gradient vibrationally boundary condition. The change in the

DOI: 10.13009/EUCASS2017-97

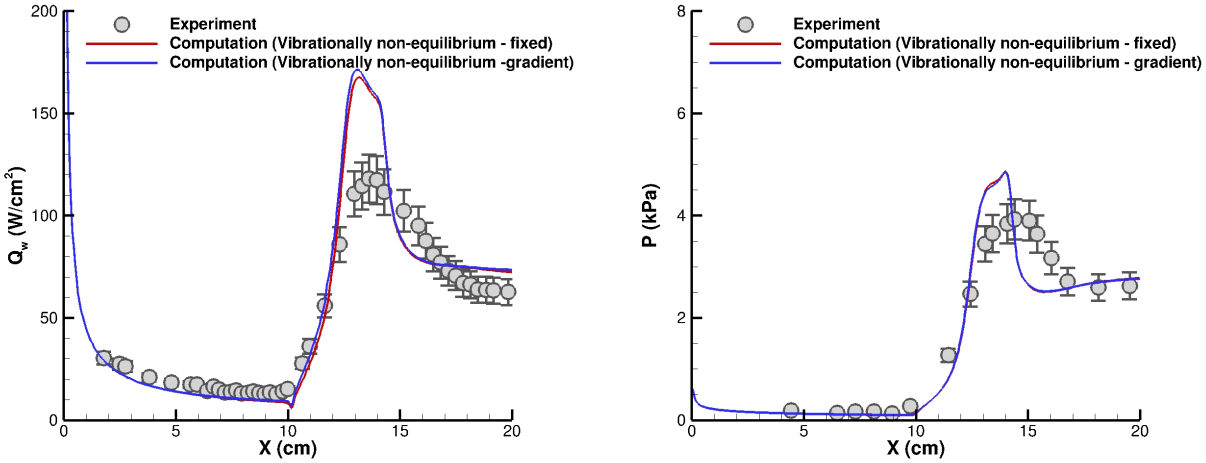

(a) Surface heat transfer (b) Surface pressure

Figure 3: Comparison with experiment for Run 2 (10.43 MJ/kg)

shape of surface pressure in the region near the peak value as a result of change in the vibrational boundary condition is more visible in this case.

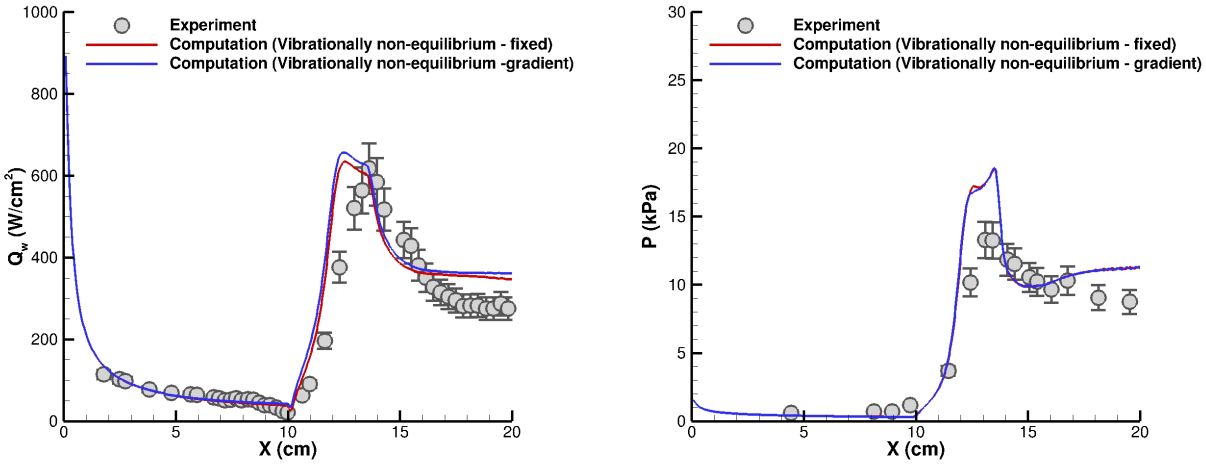

(a) Surface heat transfer (b) Surface pressure

Figure 4: Comparison with experiment for Run 5 (21.85 MJ/kg)

4.2 Analysis of Flow Structure

The Mach number contour plots of Run 2 (10.43 MJ/kg) for both vibrational boundary conditions are demonstrated in Fig. 5. The boundary layer on the cylinder generates a displacement thickness shock. This shock interacts with the flare shock. There is no separation region in the compression corner.

DOI: 10.13009/EUCASS2017-97

The Mach number contour plots of Run 5 (21.85 MJ/kg) is presented in Fig. 6. Flow structure is similar to the Run 2 (10.43 MJ/kg). There is no separation region in this calculation either.

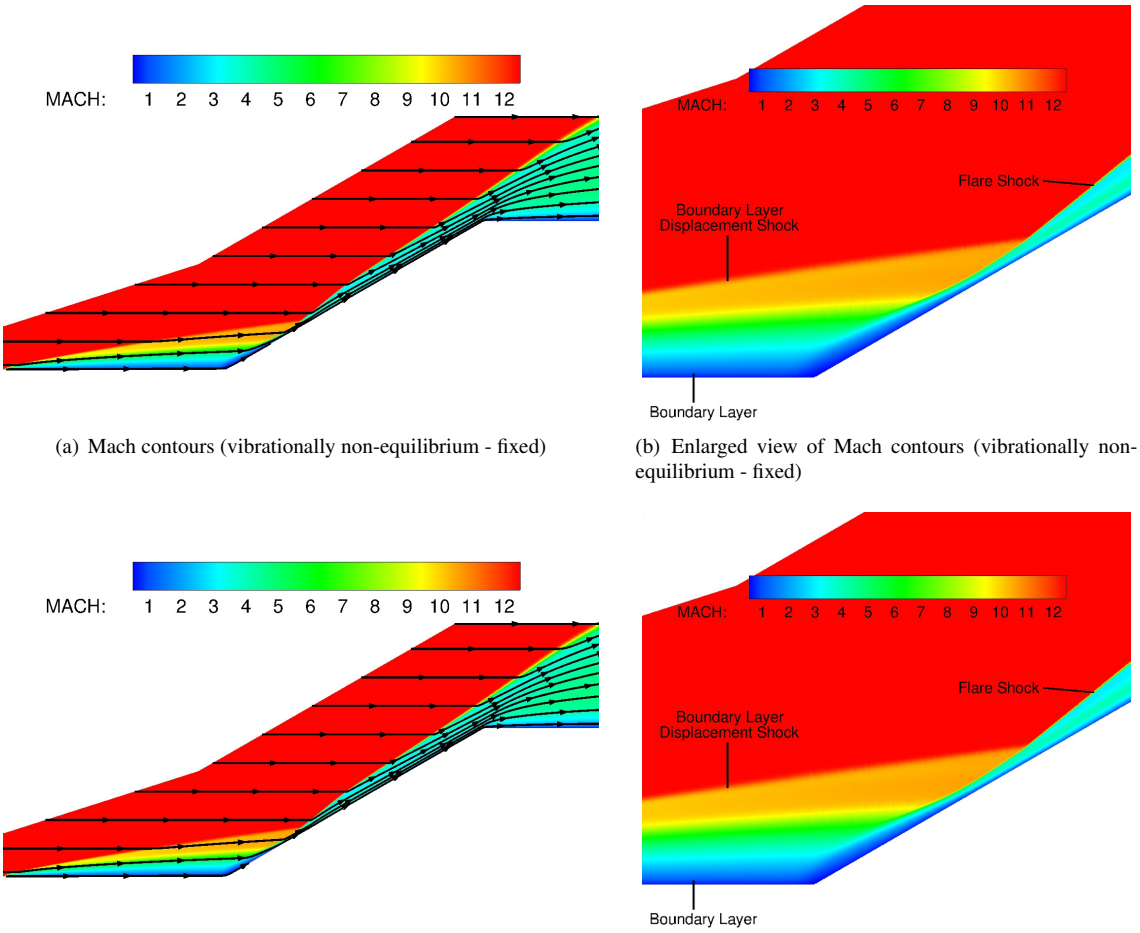

(a) Mach contours (vibrationally non-equilibrium - fixed)

(b) Enlarged view of Mach contours (vibrationally non-equilibrium - fixed)

(c) Mach contours (vibrationally non-equilibrium - gradient)

(d) Enlarged view of Mach contours (vibrationally non-equilibrium - gradient)

Figure 5: Mach contours and flow structure of Run 2 (10.43 MJ/kg)

DOI: 10.13009/EUCASS2017-97

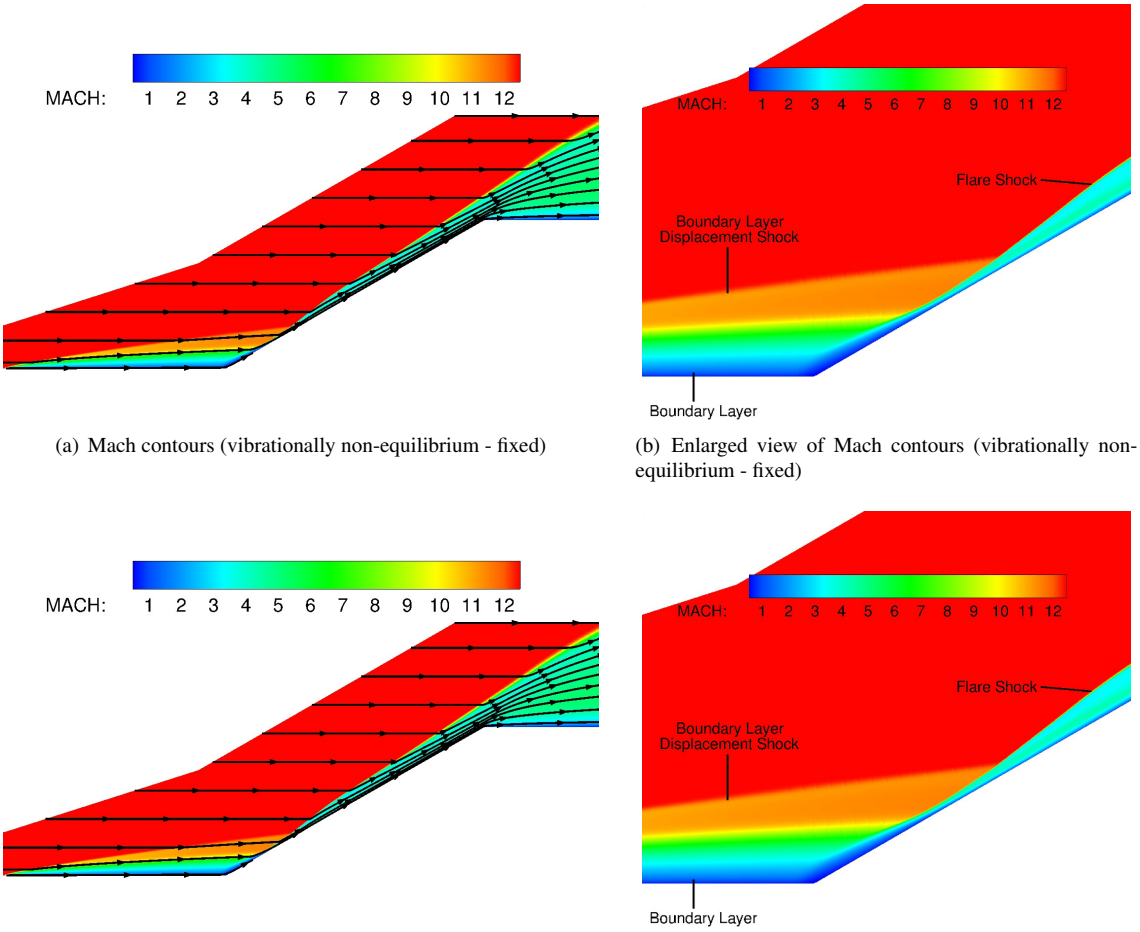

(a) Mach contours (vibrationally non-equilibrium - fixed)

(b) Enlarged view of Mach contours (vibrationally non-equilibrium - fixed)

(c) Mach contours (vibrationally non-equilibrium - gradient)

(d) Enlarged view of Mach contours (vibrationally non-equilibrium - gradient)

Figure 6: Mach contours and flow structure of Run 5 (21.85 MJ/kg)

DOI: 10.13009/EUCASS2017-97

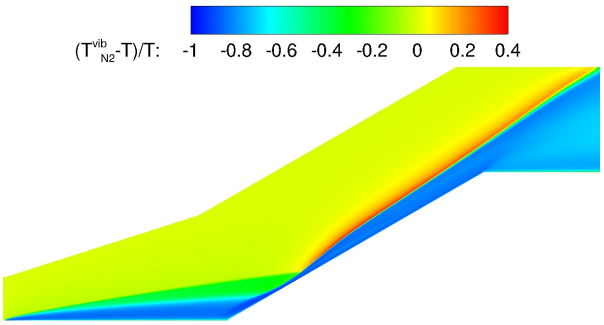

(a) N_2 vibrational temperature (vibrationally non-equilibrium - fixed)

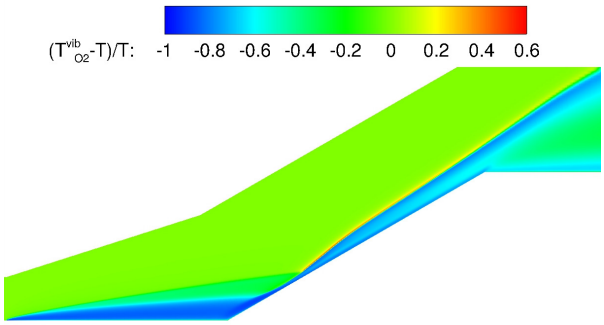

(b) O_2 vibrational temperature (vibrationally non-equilibrium - fixed)

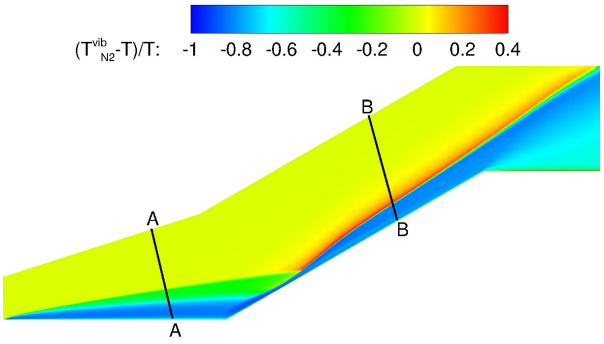

(c) N_2 vibrational temperature (vibrationally non-equilibrium - gradient)

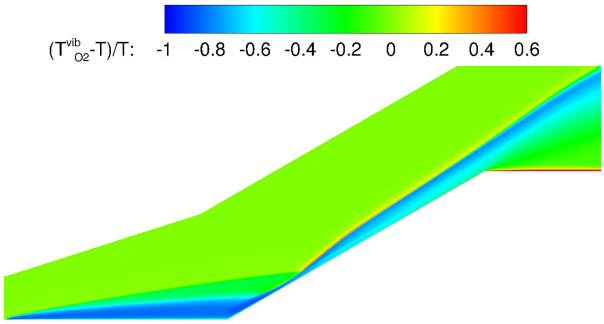

(d) O_2 vibrational temperature (vibrationally non-equilibrium - gradient)

Figure 7: Vibrational temperature of N_2 and O_2 of Run 2 (10.43 MJ/kg)

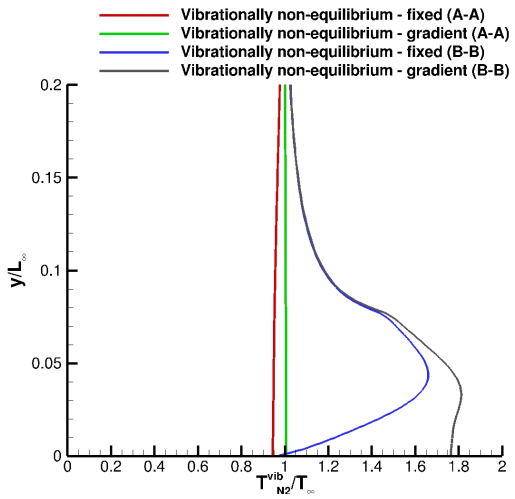

(a) N_2 vibrational temperature

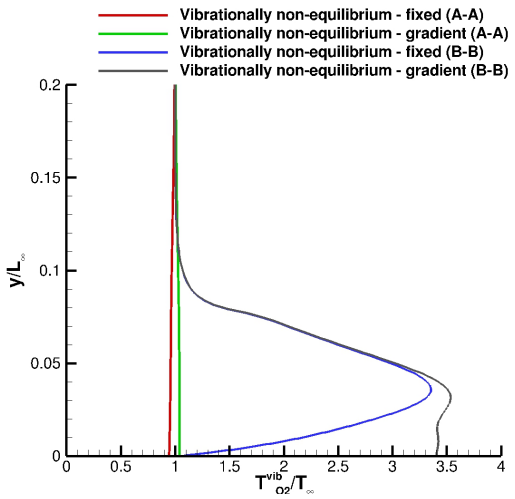

(b) O_2 vibrational temperature

Figure 8: Comparison of vibrational temperature of Run 2 (10.43 MJ/kg)

To see the effect of the vibrational boundary condition on the flow structure, the contour plots of difference of vibrational temperatures of N_2 and O_2 and the static temperature nondimensionalized by the static temperature are shown in Figs. 7 and 9 respectively for Run 2 (10.43 MJ/kg) and Run 5 (21.85 MJ/kg). The range of contour plots

DOI: 10.13009/EUCASS2017-97

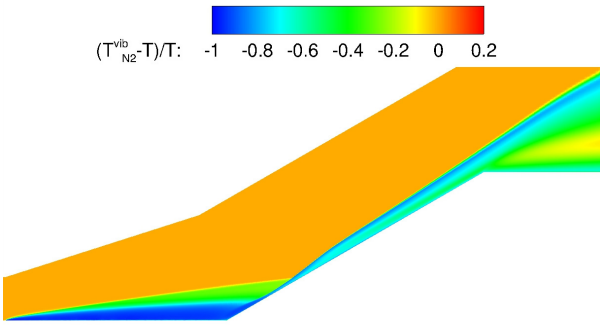

(a) N_2 vibrational temperature (vibrationally non-equilibrium - fixed)

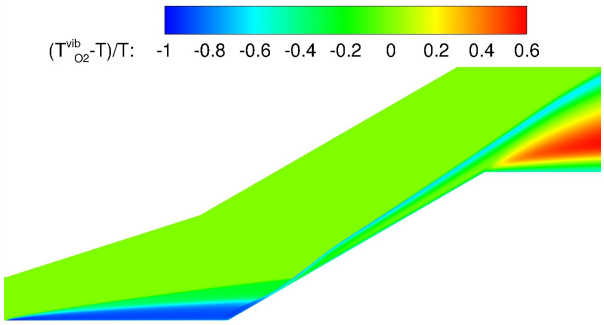

(b) O_2 vibrational temperature (vibrationally non-equilibrium - fixed)

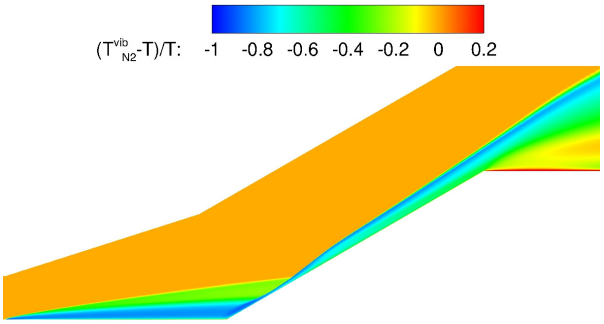

(c) N_2 vibrational temperature (vibrationally non-equilibrium - gradient)

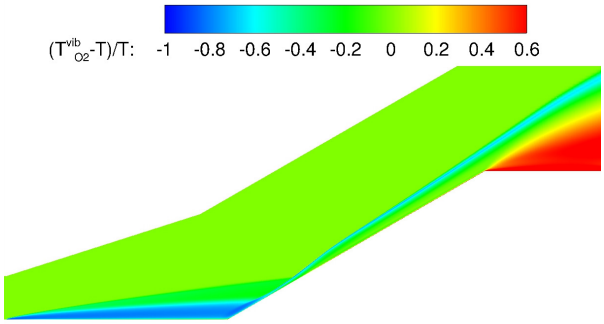

(d) O_2 vibrational temperature (vibrationally non-equilibrium - gradient)

Figure 9: Vibrational temperature of N_2 and O_2 of Run 5 (21.85 MJ/kg)

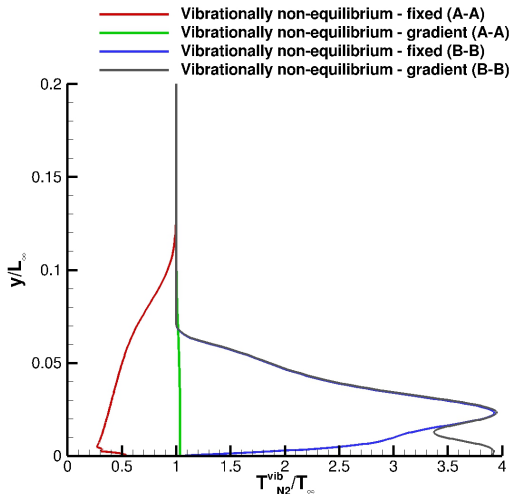

(a) N_2 vibrational temperature

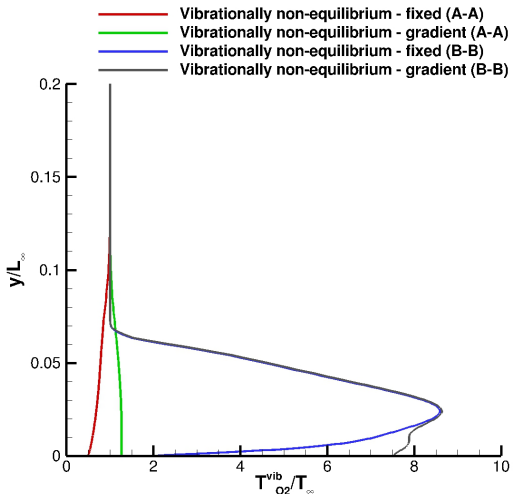

(b) O_2 vibrational temperature

Figure 10: Comparison of vibrational temperature of Run 5 (21.85 MJ/kg)

variables are fixed with the range of fixed boundary for both the fixed and zero gradient boundary conditions. In the boundary layer over the hollow cylinder, the lag of vibrational temperatures relative to the static temperature are significantly reduced specially for Run 5 (21.85 MJ/kg). Comparison of these figures shows that the zero gradient

DOI: 10.13009/EUCASS2017-97

boundary condition lead to the higher vibrational temperatures after shock waves and specifically near the walls. The higher vibrational temperature of zero gradient boundary condition compare to the fixed boundary condition is also presented in Figs. 8 and 10 shows the vibrational temperature profiles *vs.* vertical distance from the surface on lines A-A and B-B depicted in Fig. 8(c).

To better understand the effect of vibrational boundary condition at isothermal wall, we also look into the ratio of vibrational energies to the total energy. Figs. 11 and 12 show that using zero gradient condition for vibrational temperature at isothermal wall increases the vibrational energy in the domain specially in the region after the flare shock and near the wall.

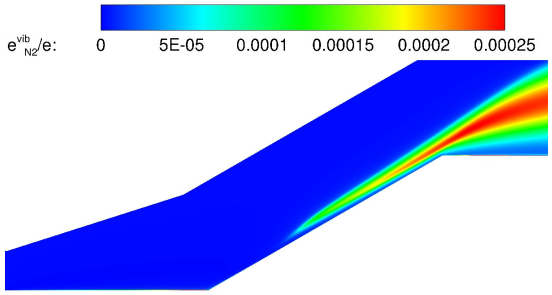

(a) N_2 energy ratio (vibrationally non-equilibrium - fixed)

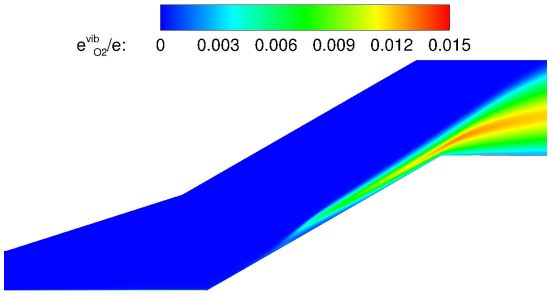

(b) O_2 energy ratio (vibrationally non-equilibrium - fixed)

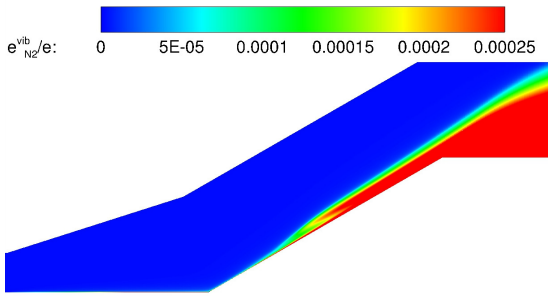

(c) N_2 energy ratio (vibrationally non-equilibrium - gradient)

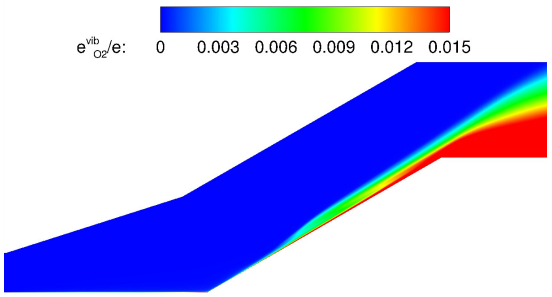

(d) O_2 energy ratio (vibrationally non-equilibrium - gradient)

Figure 11: Ratio of vibrational energy of N_2 and O_2 to the total energy for Run 2 (10.43 MJ/kg)

5. Conclusion

The effect of vibrational boundary condition at isothermal wall on the prediction of surface heat transfer and surface pressure for a hollow cylinder flare at laminar hypersonic flows and Mach numbers from 12.6 to 13.2 and stagnation enthalpies from 10.43 to 21.85 MJ/kg were examined. The two vibrational boundary conditions considered herein are 1) $T^{\text{vib}}_{\alpha}\big|_{w} = T_w$ and 2) $(\partial T^{\text{vib}}_{\alpha}/\partial n)\big|_{w} = 0$. Using $(\partial\, T^{\text{vib}}_{\alpha}/\partial n)\big|_{w} = 0$ condition leads to having higher ratio of vibrational energy near the wall after the flare shock. Despite the significant increase in the ratio of vibrational energy to the total energy, the change in the predicted peak surface pressure and peak surface heat transfer is negligible.

6. Acknowledgments

This research was supported by a grant from Emil Buehler Foundation.

DOI: 10.13009/EUCASS2017-97

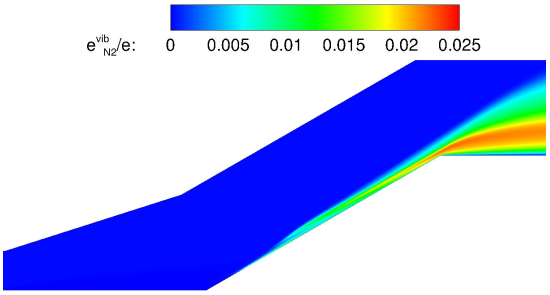

(a) N_2 energy ratio (vibrationally non-equilibrium - fixed)

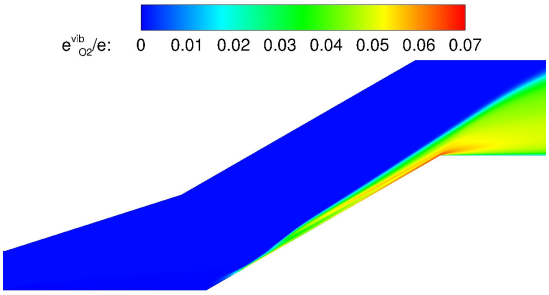

(b) O_2 energy ratio (vibrationally non-equilibrium - fixed)

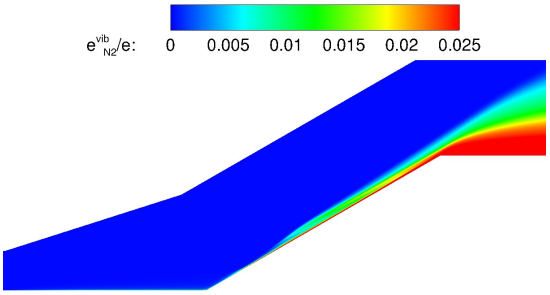

(c) N_2 energy ratio (vibrationally non-equilibrium - gradient)

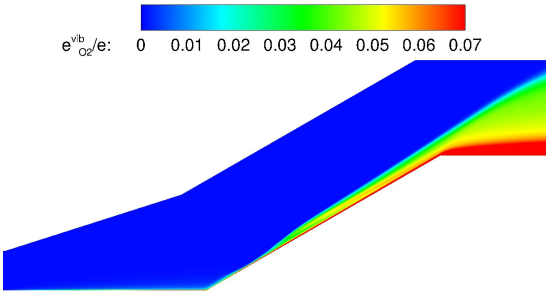

(d) O_2 energy ratio (vibrationally non-equilibrium - gradient)

Figure 12: Ratio of vibrational energy of N_2 and O_2 to the total energy for Run 5 (21.85 MJ/kg)

DOI: 10.13009/EUCASS2017-97

References

[1] GASP and GASPex version 5.1.2 reference guides. Aerosoft, Inc., Blacksburg, VA, 2014.

[2] Gasp version 5.1.2 reference guide. Aerosoft, Inc., Blacksburg, VA, 2014.

[3] National Aeronautics and Space Administration. STS-1 anomaly report. Technical Report SSVEO IFA List Date 27 February 2003, OV-103, Columbia, 2003.

[4] G Candler. Rate-dependent energetic processes in hypersonic flow. *Progress in Aerospace Sciences*, 72:37–48, January 2015. doi:10.1016/j.paerosci.2014.09.006.

[5] A Dufrene, M MacLean, R Parker, and M Holden. Experimental characterization of the LENS expansion tunnel facility including blunt body surface heating. AIAA Paper 2011-626, American Institute of Aeronautics and Astronautics, January 2011. doi:10.2514/6.2011-626.

[6] A Dufrene, M MacLean, R Parker, T Wadhams, E Mundy, and M Holden. Characterication of the new LENS expansion tunnel facility. AIAA Paper 2010-1564, American Institute of Aeronautics and Astronautics, January 2010. doi:10.2514/6.2010-1564.

[7] D Gaitonde. Progress in shock wave/boundary layer interactions. *Progress in Aerospace Sciences*, 72:80–99, January 2015. doi:10.1016/j.paerosci.2014.09.002.

[8] R Gupta, J Yos, R Thompson, and K Lee. A review of reaction rates and thermodynamic and transport properties for an 11-species air model for chemical and thermal nonequilibrium calculations to 30000 K. Reference Report 1232, NASA, 1990.

[9] J Harvey. Shock wave-boundary-layer interactions occuring in hypersonic flows in the upper atmosphere. In J Harvey and H Babinsky, editors, *Shock Wave-Boundary-Layer Interactions*, pages 336–372. Cambridge University Press, 2011. doi:10.1017/CBO9780511842757.008.

[10] N Kianvashrad and D Knight. Simulation of hypersonic shock wave-laminar boundary layer interactions. In D Knight, M. Ivanov, and I. Lipatov, editors, *Progress in Flight Physics*, volume 9 of *EUCASS Book Series, Advances in Aerospace Sciences*, pages 165–176. European Conferece for Aeronautic and space Sciences, Torus Press.

[11] N Kianvashrad and D Knight. Simulation of hypersonic shock wave laminar boundary layer interaction on hollow cylinder flare. AIAA Paper 2016-0349, American Institute of Aeronautics and Astronautics, January 2016. doi:10.2514/6.2016-0349.

[12] N Kianvashrad and D Knight. Simulation of hypersonic shock-wave-laminar-boundary-layer interaction on hollow cylinder flare. *AIAA Journal*, 55(1):322–326, January 2017. doi:10.2514/1.J055258.

[13] N Kianvashrad and D Knight. Simulation of hypersonic shock wave laminar boundary layer interaction on hollow cylinder flare, part II. AIAA Paper 2017-3975, American Institute of Aeronautics and Astronautics, June 2017.

[14] D Knight, O Chazot, J Austin, M Badr, G Candler, B Celik, D de Rosa, R Donelli, J Komives, A Lani, D Levin, I Nompelis, M Panesi, G Pezzella, B Reimann, O Tumuklu, and K Yuceil. Assessment of predictive capabilities for aerodynamic heating in hypersonic flow. *Progress in Aerospace Sciences*, 90:39–53, April 2017. doi:10.1016/j.paerosci.2017.02.001.

[15] D Knight, J Longo, D Drikakis, D Gaitonde, A Lani, I Nompelis, B Reimann, and L Walpot. Assessment of CFD capability for prediction of hypersonic shock interactions. *Progress in Aerospace Sciences*, 48–49:8–26, 2012.

[16] D Knight, H Yan, A Panaras, and A Zheltovodov. RTO WG 10: CFD validation for shock wave turbulent boundary layer interactions. RTO Technical Report TR-AVT-007-V3, NATO, January 2006.

[17] M MacLean, M Holden, and A Dufrene. Comparison between CFD and measurements for real-gas effects on laminar shock wave boundary layer interaction, I. Oral Presentation, AIAA Aviation 2014, Atlanta, GA, 2014".

[18] M MacLean, M Holden, and A Dufrene. Comparison between CFD and measurements for real-gas effects on laminar shock wave boundary layer interaction, II. Oral Presentation, AIAA Aviation 2014, Atlanta, GA, 2014.

DOI: 10.13009/EUCASS2017-97

[19] J Maus, B Griffith, and K Szema. Hypersonic Mach number and real gas effects on Space Shuttle Orbiter aerodynamics. *Journal of Spacecraft and Rockets*, 21:126–141, 1984.

[20] R Millikan and D White. Systematics of vibrational relaxation. *The Journal of Chemical Physics*, 39(12):3209–3213, 1963. doi:10.1063/1.1734182.

[21] C Park. *Nonequilibrium Hypersonic Aerothermodynamics*. John Wiley & Sons, New York, 1990.

[22] P Roe. Approximate Reimann solvers, parameter vectors, and difference schemes. *Journal of Computational Physics*, 43(2):357–372, October 1981. doi:10.1016/0021-9991(81)90128-5.

[23] W Vincenti and C Kruger. *Introduction to Physical Gas Dynamics*. Krieger Publishing Company, Malabar, Florida, 1965.

[24] C. Wilke. A viscosity equation for gas mixtures. *Journal of Chemical Physics*, 18(4):517–519, 1950. doi:10.1063/1.1747673.

[25] M Wright, D Bose, and G Candler. A data-parallel line relaxation model for the Navier-Stokes equations. *AIAA Journal*, 36(9):1603–1609, 1998. doi:10.2514/2.586.